


Article

Experimental Study on the Hydraulic Fracture Propagation in Inter-Salt Shale Oil Reservoirs

Yunqi Shen ^{1,2,3}, Zhiwen Hu ^{4,*}, Xin Chang ⁵ and Yintong Guo ⁵ 

¹ State Key Laboratory of Shale Oil and Gas Enrichment Mechanisms and Effective Development, Beijing 100083, China

² National Energy Shale Oil Research and Development Center, Beijing 100083, China

³ Petroleum Exploration and Production Research Institute, SINOPEC, Beijing 100083, China

⁴ State Key Laboratory for Coal Mine Disaster Dynamics and Control, Chongqing University, Chongqing 400044, China

⁵ State Key Laboratory of Geomechanics and Geotechnical Engineering, Institute of Rock and Soil Mechanics, Chinese Academy of Sciences, Wuhan 430071, China

* Correspondence: 202020131066@cqu.edu.cn

Abstract: In response to the difficulty of fracture modification in inter-salt shale reservoirs and the unknown pattern of hydraulic fracture expansion, corresponding physical model experiments were conducted to systematically study the effects of fracturing fluid viscosity, ground stress and pumping displacement on hydraulic fracture expansion, and the latest supercritical CO₂ fracturing fluid was introduced. The test results show the following. (1) The hydraulic fractures turn and expand when they encounter the weak surface of the laminae. The fracture pressure gradually increases with the increase in fracturing fluid viscosity, while the fracture pressure of supercritical CO₂ is the largest and the fracture width is significantly lower than the other two fracturing fluids due to the high permeability and poor sand-carrying property. (2) Compared with the other two conventional fracturing fluids, under the condition of supercritical CO₂ fracturing fluid, the increase in ground stress leads to the increase in inter-salt. (3) Compared with the other two conventional fracturing fluids, under the conditions of supercritical CO₂ fracturing fluid, the fracture toughness of shale increases, the fracture pressure increases, and the fracture network complexity decreases as well. (4) With the increase in pumping displacement, the fracture network complexity increases, while the increase in the displacement of supercritical CO₂ due to high permeability leads to the rapid penetration of inter-salt shale hydraulic fractures to the surface of the specimen to form a pressure relief zone; it is difficult to create more fractures with the continued injection of the fracturing fluid, and the fracture network complexity decreases instead.

Keywords: inter-salt shale oil; fracture propagation; fracturing fluid viscosity; in-situ stress; pumping displacement; supercritical CO₂ fracturing



Citation: Shen, Y.; Hu, Z.; Chang, X.; Guo, Y. Experimental Study on the Hydraulic Fracture Propagation in Inter-Salt Shale Oil Reservoirs. *Energies* **2022**, *15*, 5909. <https://doi.org/10.3390/en15165909>

Academic Editor: Eric James Mackay

Received: 18 April 2022

Accepted: 27 July 2022

Published: 15 August 2022

Publisher's Note: MDPI stays neutral with regard to jurisdictional claims in published maps and institutional affiliations.



Copyright: © 2022 by the authors. Licensee MDPI, Basel, Switzerland. This article is an open access article distributed under the terms and conditions of the Creative Commons Attribution (CC BY) license (<https://creativecommons.org/licenses/by/4.0/>).

1. Introduction

With the increasing demand for energy, the scale of unconventional oil and gas resource extraction has been gradually expanded. Shale gas is a typical unconventional natural gas, produced in very low-permeability, organic-rich, shale-based reservoir rock systems [1–3]. The conditions of inter-salt shale are unique, as the upper and lower compartments are salt rocks with complex lithology and low reservoir permeability, making it difficult to fracture and transform the reservoir [4–11]. Therefore, it is extremely important to explore the law of fracture expansion through the layer of inter-salt shale reservoirs, and to master the degree of reservoir transformation fracture network development and its influencing factors for inter-salt shale oil reservoir transformation [12–14].

Domestic and international scholars have carried out relevant studies on inter-salt shale oil reservoirs and the fracture expansion pattern of hydraulic fracturing. Chizhi

Xian [11] revealed the lithological characteristics of the inter-salt reservoirs in the depression through the lithological description of dolomite in the Qianjiang inter-salt shale oil reservoirs, combined with the geochemical characteristics of inter-salt muddy dolomite. Shizhao Dai [15,16] found that the inter-salt formation is a sediment located in the relative desalination conditions of salt lake waters in the salt-bearing rhyolite formation in the south-central part of the depression, and the salt-bearing rhyolite formation is a mixture of carbonate, sulfate and mudstone, frequently interacting with the inter-salt formation. The inter-salt layer is doubly influenced by chemical deposition and mechanical deposition, the chemical rocks and clastic rocks are alternately interbedded at millimeter or even micron level, and the rock types are more complex. Chen Bo [17] compared the deposition and salt rhythm characteristics of the Qianjiang Formation in the Qianjiang Depression and the Shashi Formation in the Jiangling Depression, and obtained that the salt formation of the Qianjiang Formation is a gray salt rock with a small amount of associated minerals such as aragonite, and the rock types of the inter-salt layer include mud dolomite, dolomitic mudstone, aragonite-bearing dolomite, mudstone and oil shale. Zhengming Yang et al. [18] conducted a study and evaluation related to salt dissolution in salt rock compartments in inter-salt shale and found that the pore volume, porosity and permeability of salt rock compartments increased after salt dissolution. Several different model compounds were also selected to simulate the chemical changes in crude oil components and to propose the reaction mechanism. N.R. Warpinski [19,20] et al. studied the influence law of hydraulic fracture through the interlayer. S. C. Blair [21] et al. suggested that when a hydraulic fracture expands in a vertical discontinuity, the fluid will first penetrate along the interface, and after penetrating a certain distance on the interface, the hydraulic fracture will break through the interface and continue to expand in the original direction. T. L. Blanton [22,23] investigated the effect of natural fractures on hydraulic fracture extension by indoor triaxial hydraulic fracturing tests in shales containing natural fractures, and concluded that hydraulic fractures would continue to extend through natural fractures only under high stress differences and large approach angles, while, in most cases, hydraulic fractures would stop or turn at natural fractures. A. A. Daneshy [24] conducted a theoretical and experimental study on the expansion law of hydraulic fractures in layered formations, pointing out that strong interfaces do not prevent fracture expansion, while the law of weak interfaces preventing fracture expansion does not change with the change in the nature of the strata on both sides of the interface. Relatively few domestic scholars have studied this area. Chen Zhixi [25] and others applied the theory and method of rock mechanics to establish a numerical model of hydraulic fracture vertical extension in laminated media, and the research results showed that the ground stress profile is the main factor affecting the range and direction of fracture vertical extension, the fracture toughness of the rock formation has a significant fracture-stopping effect on fracture vertical extension, and the flow pressure drop in the fracturing fluid along the direction of the fracture height has a large influence on the fracture height. Under certain stratigraphic conditions, whether the fracture extends to the compartment and the size of the extension mainly depend on the operating pressure. By introducing an additional enhancement term in the interpolation function of displacement to achieve fracture extension independent of the grid boundary, Su-Ling Wang [26] et al. obtained the extension law of fractures through the sand/mudstone interface. Moreover, the fracture extension at the sand/mudstone interface of a low-permeability reservoir was tracked in real time using a white light scattering experiment, and the fracture extension process was in good agreement with the numerical simulation process, indicating that the extended finite element method is an effective means to quantitatively analyze the fracture extension, while the influencing factors of the fracture extension through the interface were also analyzed.

From the above studies, it can be seen that most of the current research on inter-salt shale oil reservoirs is focused on the microscopic mineral composition and lithological characteristics, while most of the studies on the hydraulic fracture expansion law are focused on sandstone and mudstone interfaces, and there are fewer studies on the expansion

law of hydraulic fractures through layers in inter-salt shale. To this end, it is necessary to carry out real triaxial hydraulic physical simulation experiments with actual cores downhole, and to systematically study the hydraulic fracture expansion law and influence mechanism of inter-salt shale hydraulic fractures with fracturing fluid viscosity, ground stress and fracturing fluid discharge as variables, so as to optimize the hydraulic fracture extraction design of inter-salt shale oil reservoirs and improve the reservoir recovery rate.

2. Materials and Methods

2.1. Equipment

Based on the conventional three-axis rock mechanics test machine, a set of cylindrical fracturing physical simulation test systems was implemented, as shown in Figure 1.

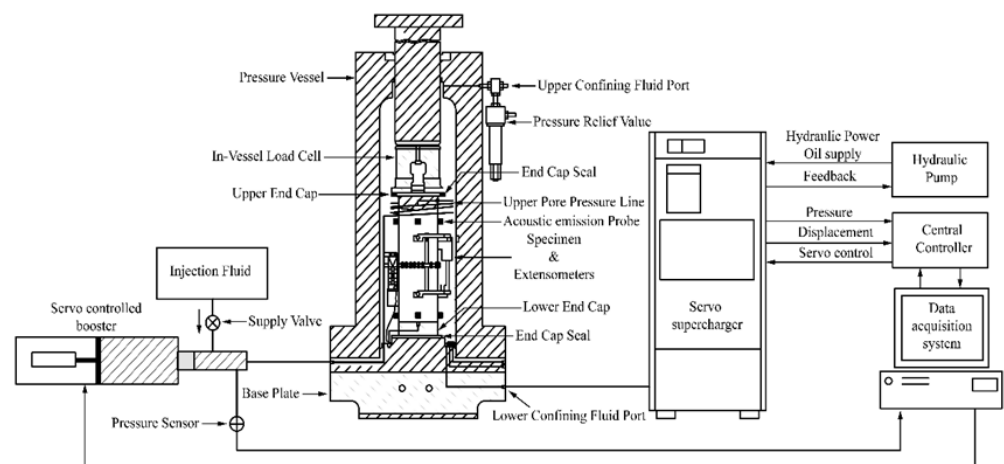


Figure 1. Schematic diagram of a full diameter core fracturing physical simulation experimental device.

The test system is mainly composed of a rock stress servo loading system, a fracturing fluid injection system and a sound emission detection system. Among them, the rock stress servo loading system is mainly used to provide the stress state in deep shale, simulating the real stress environment of the formation; the fracturing fluid injection system is mainly injecting the fracturing in the sample to simulate a wellbore in a constant voltage/constant flow mode liquid, and realize the real-time acquisition of pump pressure and displacement; the acoustic emission detection system is mainly used to detect micro-crack signals in the rock hydraulic fracturing process and obtain hydraulic cracks and spatial features in real time.

2.1.1. Rock Stress Servo Loading System

The rock stress servo loading system is mainly composed of a full digital electro-hydraulic servo rock triaxial test system, as shown in Figure 2. The system mainly includes the following: core high pressure triaxial chamber, servo hydraulic source, servo supercharger, door character rigid frame, radial/axial strain, warming system, and digital acquisition system. The maximum output axial force is 2000 KN, and the maximum working confining pressure is 140 MPa, which can better meet the requirements of the stress of the shale oil reservoir; at the same time, the sample is equipped with a sample heating device, the constant temperature system, and the upper limit temperature is 100 °C. Maximum allowable specimen size is 100 mm × height of 200 mm in diameter and equipped with axial/radial strain regulations, resolution 0.0001 mm.

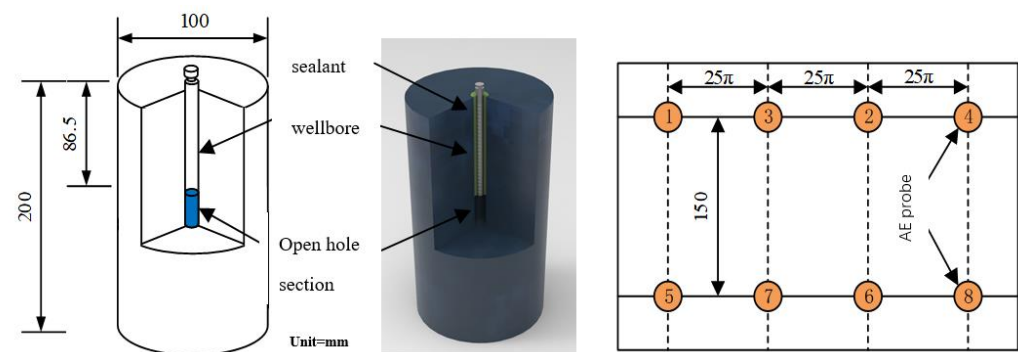


Figure 2. Schematic diagram of full sample and acoustic emission probe.

2.1.2. Fracturing Fluid Pump Injection System

The fracturing liquid pump is mainly used to provide a high-pressure fracturing fluid of constant flow. In order to provide more accurate flow control than most reciprocating pumps, this test system uses the US Teledyne (Thousand Oaks, CA, USA) Isco-260HP high-precision high-pressure plunger pump as the power source of fracturing fluid. Isco-260HP plunger pump maximum capacity 266 mL, output displacement 0.001–107 mL/min, measurement accuracy $\pm 0.5\%$ (maximum leakage amount is 0.50 $\mu\text{L}/\text{min}$); the maximum output pressure is 65.5 MPa, and the measurement accuracy is 0.1%.

2.1.3. Acoustic Emission Detection System

The acoustic transmitting detection system is mainly composed of a host, sensor, preamplifier, acquisition card, and AEWIN signal acquisition and analysis software with five major modules.

The selection of the acoustic emission sensor has an important influence on the detection result. The acoustic emission probe selected in this test is the SR40M low-frequency narrow-bandwidth probe produced by Beijing Sonhua Xingye Technology Co., LTD (Beijing, China). The performance parameters are as follows: frequency range 15 KHz–75 KHz, resonant frequency 400 KHz, and sensitivity peak >75 dB.

Since the acoustic transmission sensor has a higher output impedance, the output signal current is weak, and it is not suitable for long-distance transmission. Therefore, it is necessary to connect the front amplifier to enlarge the voltage signal of the sensor to the capture card. The acoustic emission preamplifier used in this trial is a 2/4/6 amplifier produced by the American Physical Acoustic Corporation (PAC) (Lansing, MI, USA), and the gain is 20,40,60 dB three-stop, which is powered by a PAC sound emission card.

The core components of the acoustic emission detection system consist of 8 PCI-2-type sound acquisition cards. PCI-2 is a high-performance/low-cost position-transmitting capture card developed by PAC, which is 40 MHz, with an 18-bit A/D converter, which can perform real-time analysis and higher signals. Treatment accuracy, minimum noise threshold value 17 dB. In addition, the PCI-2 system has a unique waveform stream data storage function that continuously deposits the hard disk at a rate of 10 m per second. A layer of acoustic coupling agent is applied to the sound emission probe during the test, ensuring that the probe is closely coupled to the surface of the sample.

2.2. Preparation of Materials

The samples used in this experiment are the core and shale outcrop in the 4th dip of well Bangye Oil 2, which contains a large amount of salt rock interlayer bands. First, as shown in Figure 2, the core is processed into a cylindrical sample of $\phi 100$ mm \times 200 mm specification and the outer diameter of the sample is processed evenly by a lathe. The sample center drills a blind hole having a diameter of 12 mm as the simulated wellbore, and is buried in an outer diameter of 6.0 mm, with a stainless steel pipe of a wall thickness of 1.5 mm as an analog sleeve, and the annular gap is subjected to sealing treatment.

2.3. Experimental Method

In this experiment, the influence of fracturing fluid viscosity, in-situ stress, and fracturing fluid displacement on the hydraulic fracture propagation law of an inter-salt shale oil reservoir is analyzed with the control variable method. This experiment has carried out 10 sets of cylindrical sample water pressure tests. The specific parameters of each sample are shown in Table 1, and sample numbers and test conditions are shown in Table 2.

Table 1. Sample-specific parameters.

No.	Sample No.	Length/mm	Diameter/mm	Quality/g
1	2418	49.88	98.94	500.94
2	2985	49.54	108.64	536.084
3	2988	49.24	101.42	490.268
4	3665	49.12	108.02	519.248
7	1933	49.06	100.3	490.36
8	1956	49.24	99.86	491.832
9	25-SC	98.88	201.124	3955.308
10	26-SC	98.88	199.28	3949.955
11	27-SC	99.6	198.93	4031.648
12	28-SC	99.08	196.28	3845.258

Table 2. Full diameter core three-axis fracturing test experiment.

No.	Sample No.	Fracturing Medium	Axial Stress/MPa	Perimure Pres-sure/MPa	Solid Discharge (mL/min)	Remark
1	2418	Slippery	29	25	4.8	BY-2
2	2985		29	25	7.2	
3	2988		29	25	4.8	
4	3665		29	25	7.2	
7	1933	Supercritical CO ₂	29	25	4.8	
8	1956		29	25	7.2	
9	25-SC	Supercritical CO ₂	28	25	6.0	Shale outcrop
10	26-SC		31	28	6.0	
11	27-SC		18	15	6.0	
12	28-SC		28	25	1.2	

The specific steps of this experiment are as follows:

- (1) Description before hydraulic fracturing: We observe the sample layer and natural crack development with the naked eye, and identify the weak distribution of the original structure by chalk or marker.
- (2) Gas tight inspection: Because the shale layer is more developed, it is very prone to shear damage during the preparation of the sample, causing wellbore sealing damage, so, before the experiment, we pump a certain amount of fluid into the wellbore, and the pressure is maintained at around 0.5 MPa, for 3–5 min, and we observe whether there is a fracturing liquid in the sample surface.
- (3) Acoustic emission probe installation: Eight acoustic emission probes are installed on the surface of the sample, and the probes are tightly bonded with the sample with a coupling agent, while gently tapping each probe to ensure that each probe can work normally.
- (4) Stress loading: We place the sample in a three-axis high-pressure chamber, sequentially load the peripheral pressure and axial pressure to the specified value, and maintain for 10–20 min to ensure that the internal force is uniform.
- (5) Fracturing fluid injection: We start the Isco plunger pump, inject the fracturing fluid inside the sample according to the set displacement, and synchronously operate the sound emission detection; when the pump pressure has dropped significantly, we

close the plunger pump and sound emission detection system, and remove the axial pressure and peripheral sequential.

- (6) Description after hydraulic fracturing: At the end of the experiment, a digital camera is first used to photograph the sample surface and record the surface cracks. Then, we select a partial sample to conduct a CT sweep surface, quantitatively characterize the spatial distribution of hydraulic cracks, and finally take the test sample after the test, and the hydraulic crack is displayed; then, we summarize the hydraulic crack expansion.

3. Results

3.1. Slippery Water Fracturing Fluid

Two sets of indoor slick water fracturing physical simulation experiments were carried out with core samples from Well Bengyeyou 2. The experimental results are shown in Table 3.

Table 3. Summary of physical simulation test results of slick water fracturing.

No.	Sample No.	Fracturing Medium/MPa	Axial Stress/MPa	Solid Discharge (mL/min)	Burst Pressure/MPa	Pump Pressure Curve Characteristics	Crack Propagation Pattern
1	2418	29	25	4.8	27.57	It rises rapidly before the peak, and then quickly falls to the confining pressure after the peak.	Form 1 horizontal bedding seam.
2	2985	29	25	7.2	30.97	Rapid rise before the peak, obvious fluctuation after the peak, and gradually reduced to confining pressure.	Open multiple horizontal bedding seams.

The number of sample 1 is 2418, which is taken from Well Bengyeyou 2 and is a shale core with well-developed bedding. The photos and CT scan results of the sample before the experiment are shown in Figure 3. From the CT scanning results of the core before the experiment, it can be seen that the inter-salt shale is extremely developed due to the bedding, and some beddings are opened due to the stress release of the downhole core. Before the experiment, a layer of black epoxy resin glue was evenly spread on the surface of the core to prevent damage to the sample caused by external disturbance.



Figure 3. Core photos and CT scan results of sample 1 before the experiment.

Under the conditions of confining pressure of 25 MPa, axial force of 29 MPa and displacement of 4.8 mL/min, the hydraulic fracturing physical simulation experiment was carried out by using slick water fracturing fluid with viscosity of 3 MPa·s, and the fracture pressure of the sample was 27.57 MPa. Figure 4 shows the fracture morphology photos and CT scan results of sample 1 after the test. During the fracturing process, the hydraulic fractures started from the bottom of the well and expanded, and then extended to the open bedding surface near the bottom of the well and then turned to the edge of the well. As the bedding plane expands, a horizontal bedding fracture is formed near the bottom of the well.



Figure 4. Core photos and CT scan results of sample 1 after the experiment.

The acoustic emission and pump pressure curves of sample 1 are shown in Figure 5. The pump pressure curve can be divided into three distinct stages: 0–760 s is the stable injection stage; 760–890 s is the fracture initiation and development stage; 890–980 s is the post-peak fracture expansion stage. In the initial stage, with the injection of fracturing fluid, some micro-cracks at the bottom of the well were damaged and a small amount of acoustic emission events occurred, and the energy was lower than 100 mV·ms. When the injection time lasted 760 s, the acoustic emission energy curve began to rise rapidly, indicating that the initiation point appeared and the hydraulic fracture began to develop. When the bottom hole pressure continued to rise to the fracture pressure of 27.57 MPa, the macroscopic damage of the sample occurred, and then the pump pressure curve rapidly decreased to the size of the confining pressure. Since the fracturing is slightly smaller than the axial stress, it shows that the hydraulic fractures are linked to the bedding fractures that were originally opened during the expansion process. As fracturing fluid continues to be injected, more bedding surfaces expand and open. Due to the limitation of confining pressure, the energy accumulated in the early stage is rapidly released to the surroundings in the form of elastic waves, and the peak of acoustic emission energy begins to appear intensively.

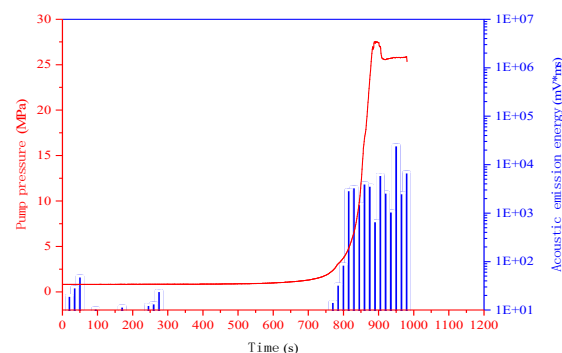


Figure 5. Pump pressure and acoustic emission characteristic curve of sample 1.

Sample 2 is numbered 2985, which is taken from Well Bengyeyou 2 and is a shale core with well-developed bedding. Figure 6 shows the photo of the sample before the experiment. As in the case of sample 1, some beddings of the downhole core were opened due to stress release. Before the experiment, a layer of black epoxy resin glue was evenly applied to the surface of the lower half of the core to prevent external disturbance from damaging the sample and thus affecting the experimental results.

Under the condition that the confining pressure is 25 MPa, the axial force is 29 MPa, and the displacement is 7.2 mL/min, the hydraulic fracturing physical simulation experiment is carried out with slick water fracturing fluid with a viscosity of 3 MPa·s, and the fracture pressure of the sample is obtained, which is 30.97 MPa. The characterization of crack morphology after the test of sample 2 is mainly described based on the acoustic emission localization results. Figure 7 shows the fracture morphology photo and AE positioning

effect of sample 2 after the test. The acoustic emission events are mainly concentrated at the bottom of the well, and several acoustic emission event points are scattered vertically, indicating that, during the hydraulic fracturing process of sample 2, the hydraulic fractures start from the bottom of the well and expand longitudinally. During the expansion process, the opened bedding plane turns to expand along the direction of the bedding plane and continues to expand vertically, opening a number of horizontal bedding fractures.

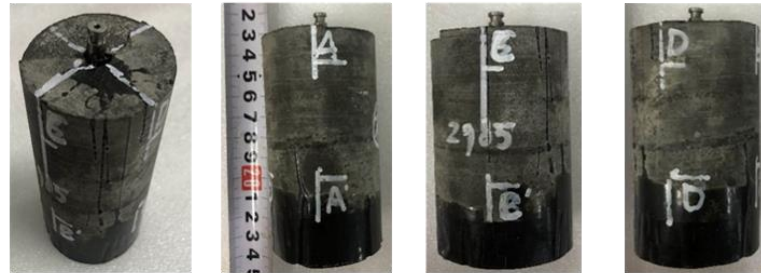


Figure 6. Core photos and CT scan results of sample 2 before the experiment.

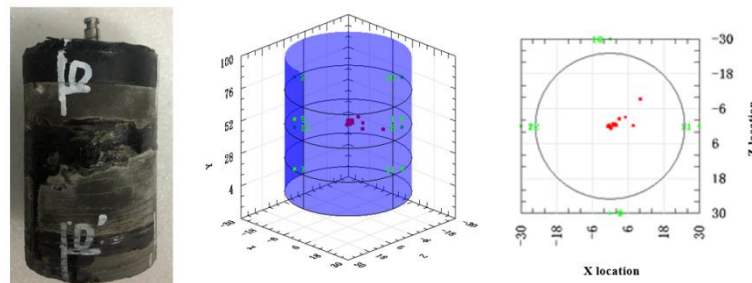


Figure 7. Core photos and AE positioning renderings of sample 2 after the experiment.

The acoustic emission and pump pressure curves of sample 2 are shown in Figure 8. Here, 0–150 s is the stable fluid injection stage, and the fracturing fluid is continuously injected into the bottom of the well, resulting in pressure hold-up at the bottom of the well. At 150 s, the pump pressure curve began to rise rapidly, and at 200 s, the bottom hole pressure reached the peak rupture pressure, the rupture pressure was 30.97 MPa, and the sample suffered macroscopic damage. Moreover, 200–500 s is the crack propagation stage. After the peak, the pump pressure curve did not drop rapidly to the confining pressure, but showed a sawtooth fluctuation. At the same time, the acoustic emission energy continued to maintain a high level, which was due to the macroscopic damage of the sample. After this, the continuous injection of fracturing fluid resulted in the continuous opening of a large number of bedding fractures and micro-fractures. The bedding cracks and micro-cracks opened in 500–640 s extended to the surface of the sample, and the pump pressure curve quickly dropped to the confining pressure.

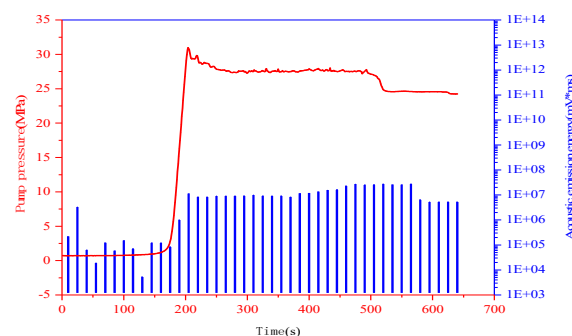


Figure 8. Pump pressure and acoustic emission characteristic curve of sample 2.

3.2. Guar Gum Fracturing Fluid

An indoor guar gum fracturing physical simulation experiment was carried out using cores from Well Bengye 2 and Diving 4. The experimental results are shown in Table 4.

Table 4. Summary of results of guar gum fracturing physical simulation experiments.

No.	Sample No.	Fracturing Medium/MPa	Axial stress/MPa	Solid Dis-charge(mL/min)	Burst Pressure/MPa	Pump Pressure Curve Characteristics	Crack Propagation Pattern
3	2988	29	25	4.8	27.89	The pre-peak rises approximately linearly, and the post-peak rapidly drops to the confining pressure.	Open multiple horizontal bedding seams.
4	2985	29	25	7.2	32.35	The pre-peak rises approximately linearly, and the post-peak gradually decreases to the confining pressure.	Open multiple horizontal bedding seams.

Sample 3 is No. 2988. This sample is taken from Well Bengyeyou 2. It is a bedded shale core. The photos and structure of the sample before the experiment are shown in Figure 9. Some thin salt rocks can be seen on the surface of the sample in the form of sandwich strips.

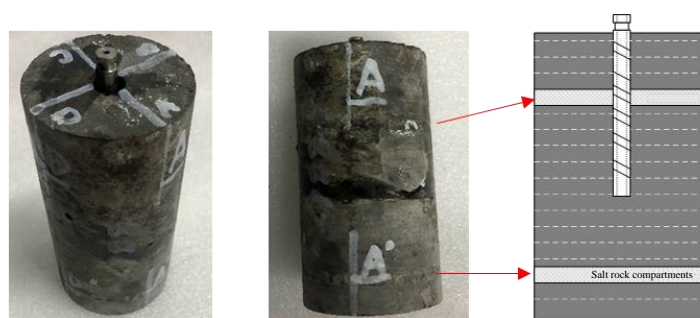


Figure 9. Core photo of sample 3 before experiment.

Under the condition that the confining pressure is 25 MPa, the axial force is 29 MPa, and the displacement is 4.8 mL/min, the hydraulic fracturing physical simulation experiment is carried out with guar gum fracturing fluid with a viscosity of 120 MPa·s, and the rupture pressure of the sample is obtained, which is 27.89 MPa. The crack morphology characterization of sample 3 after the test is mainly described based on the acoustic emission localization results. Figure 10 shows the fracture morphology photos and AE positioning effect of sample 3 after the test. The acoustic emission events are mainly concentrated at the bottom of the well, and some acoustic emission event points appear along the bedding plane of the sample, indicating that sample 3 is in the process of hydraulic fracturing; hydraulic fractures start from the bottom of the well and expand longitudinally. During the expansion process, the bedding plane formed by the thin interlayer strip of salt rock turns to expand in the direction of the bedding plane, while the hydraulic fracture continues longitudinally, expanding and communicating with more bedding planes, and opening up multiple horizontal bedding seams.

The acoustic emission and pump pressure curves of sample 3 are shown in Figure 11. The pump pressure curve can be divided into three distinct stages: 0~540 s is the stable injection stage; 540~570 s is the fracture initiation and development stage; 570~720 s is the post-peak fracture expansion stage. In the initial stage, the fracturing fluid is continuously injected at the bottom of the well to form pressure suppression, the pump pressure curve changes gently, and the micro-fractures at the bottom of the well are damaged and a large number of acoustic emission events occur. When the injection time continued to 540 s, the pump pressure curve began to rise rapidly, indicating that the crack initiation point appeared, and the hydraulic fractures began to develop and expand; when the bottom hole

pressure continued to rise to the fracture pressure of 27.89 MPa, the macroscopic damage of the sample occurred, and then after the peak, the pump pressure dropped rapidly to the level of the confining pressure. The fracturing of sample 3 is also slightly smaller than the axial stress, which also shows that the hydraulic fractures communicate with the bedding fractures formed by the thin interlayer strips of the salt rock during the expansion process; the pump pressure curve remains at the level of the confining pressure, and the energy accumulated in the early stage is rapidly released to the surroundings in the form of elastic waves, and high acoustic emission energy still appears.

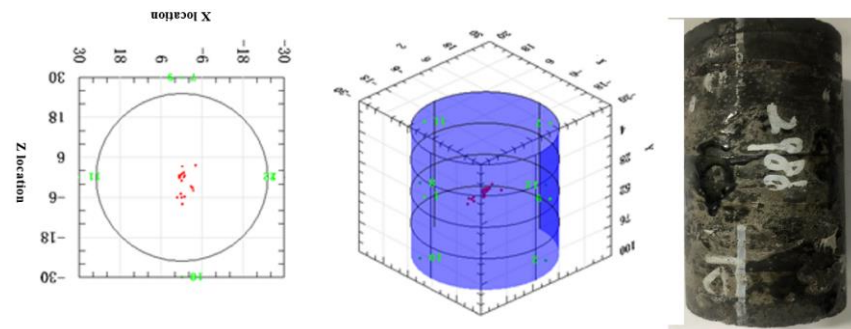


Figure 10. Core photos and acoustic emission location results of sample 3 after the experiment.

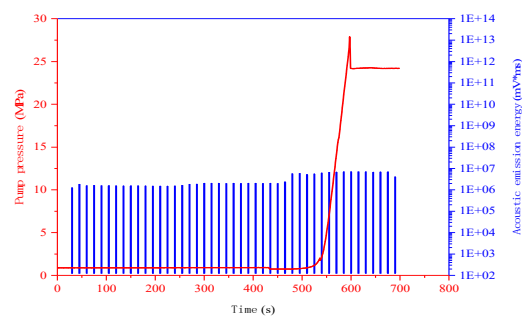


Figure 11. Pump pressure and acoustic emission characteristic curve of sample 3.

Sample 4 is No. 3665. This sample is taken from Well Bengyeyou 2. It is a bedded shale core. The photo of this sample before the experiment is shown in Figure 12. On the same surface as in sample 3, some thin salt rocks can be seen with the naked eye, in the form of sandwich strips.



Figure 12. Core photos of sample 4 before the experiment.

Under the condition that the confining pressure is 25 MPa, the axial force is 29 MPa, and the displacement is 7.2 mL/min, the hydraulic fracturing physical simulation experiment is carried out with guar gum fracturing fluid with a viscosity of 120 mPa·s, and the fracture pressure of the sample is obtained, which is 32.35 MPa. The fracture morphology and acoustic emission location after the experiment are shown in Figure 13. The acoustic emission events are mainly concentrated at the bottom of the well, and some acoustic emission event points appear along the bedding plane, indicating that the fractures start

from the bottom of the well and expand along the longitudinal direction. At the same time, the direction and expansion occurred along the bedding plane, and the communication opened up multiple bedding seams. The CT scan results of sample 4 after pressing are shown in Figure 14. The same verification shows that multiple horizontal bedding seams are opened inside the sample after pressing.

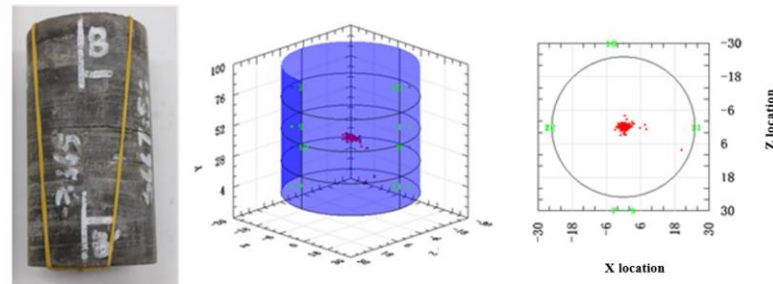


Figure 13. Core photos and acoustic emission location results of sample 4 after the experiment.

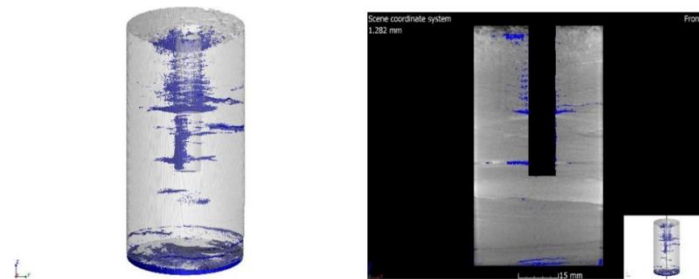


Figure 14. CT scan results of sample 4 after the experiment.

Figure 15 shows the acoustic emission and pump pressure curves of sample 4. The pump pressure curve of 0~55 s is flat. The fracturing fluid is injected at the bottom of the well to form pressure suppression, and the micro-fractures at the bottom of the well are damaged, resulting in a large number of acoustic emission events. When the injection time lasted for 55 s, the pump pressure curve rose rapidly to the rupture pressure of 32.35 MPa, and the sample was macroscopically damaged, and then the pump pressure quickly dropped to the confining pressure, and the fracturing fluid continued to be injected. Acoustic emission energy continues at high levels.

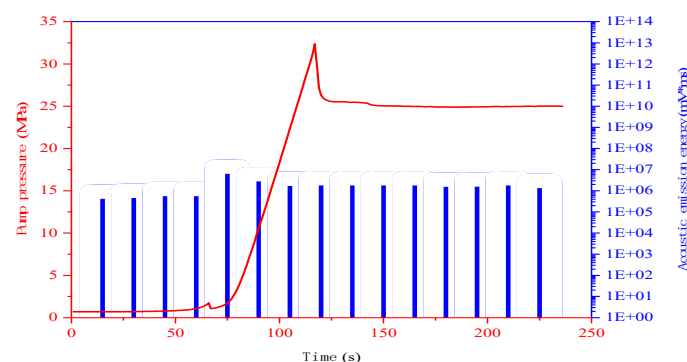


Figure 15. Pump pressure and acoustic emission characteristic curve of sample 4.

3.3. Supercritical Carbon Dioxide Fracturing Fluid

Indoor supercritical carbon dioxide fracturing physical simulation experiments were carried out with cores and shale outcrops from Well Bengye 2, respectively. The experimental results are shown in Table 5.

Table 5. Summary of results of physical simulation experiments of supercritical carbon dioxide fracturing.

No.	Sample No.	Fracturing Medium /MPa	Axial Stress /MPa	Solid Discharge (mL/min)	Burst Pressure /MPa	Pump Pressure Curve Characteristics	Crack Propagation Pattern
5	1933	29	25	4.8	37.55	The pre-peak pump pressure curve rises slowly, and the post-peak curve rapidly drops to the confining pressure.	Forming a curved longitudinal crack.
6	1956	29	25	7.2	50.77	The pre-peak pump pressure curve rises slowly before the peak, and the post-peak curve rapidly drops to the confining pressure.	Forming a curved longitudinal crack.
7	25-SC	28	25	6.0	37.4	The pre-peak rises slowly, and the post-peak curve rapidly drops to the confining pressure.	Generate 1 longitudinal main fracture and open 2 bedding fractures.
8	26-SC	31	25	6.0	52.6	The pre-peak rises slowly, and the post-peak curve rapidly drops to the confining pressure.	Generate 1 longitudinal main fracture and open 2 bedding fractures.
9	27-SC	18	15	6.0	31.6	The pre-peak rises slowly, and the post-peak curve rapidly drops to the confining pressure.	Generate 1 longitudinal main fracture and open 2 bedding fractures.
10	28-SC	28	25	1.2	34.5	The pre-peak rises slowly, and the post-peak curve rapidly drops to the confining pressure.	Generate 1 longitudinal main fracture and open 2 bedding fractures.

Sample 5 is No. 1933. This sample is taken from Well Bengyeyou 2 and is argillaceous dolomite. The photo of this sample before the experiment is shown in Figure 16. The surface of the sample can be seen with glauconite and other mineral-filled belts, which are not observed. There is an obvious bedding seam, and the integrity of the sample is good.

**Figure 16.** Core photos of sample 5 before the experiment.

The experimental confining pressure of the sample is set to 25 MPa, the axial force is 29 MPa, the displacement is 4.8 mL/min, supercritical CO₂ is used as the fracturing medium, and the sample rupture pressure is 37.55 MPa.

The crack morphology and acoustic emission location after the experiment are shown in Figure 17. Since there is no obvious bedding surface in the sample, the horizontal bedding crack is not opened after the sample is pressed, a curved longitudinal through-crack is formed, and the sample is split. The crack propagation path is mainly affected by the stress conditions; the glauconite transition zone is developed in the lower part of the sample, and the crack propagation direction is bent due to the lithological heterogeneity. In addition, the crack surface of the sample was visually observed, and the crack surface was rough, showing the characteristics of obvious tensile failure.

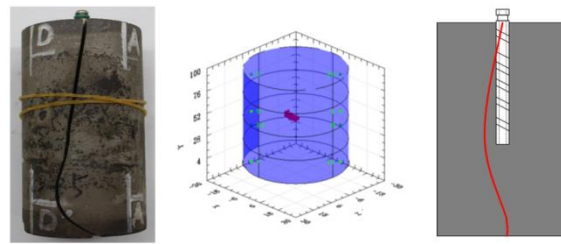


Figure 17. Core photos and acoustic emission location results of sample 5 after the experiment.

The acoustic emission and pump pressure curves of the samples are shown in Figure 18. The pump pressure curve of sample 5 can be divided into the following three stages, as follows. ① 0~200 s—in the initial stage of fracturing, due to the existence of wellbore cavities and primary fractures, the initial carbon dioxide preferentially enters such large spaces; at this stage, the number of acoustic emission events is small, and it can be considered that no new pores and cracks are generated. ② 200~1550 s—in the wellbore pressure holding stage, CO₂ changes from the wellbore filling stage to the wellbore pressure holding stage; due to the strong compressibility of carbon dioxide, the growth trend of the pressure–time curve is relatively gentle. In order to shorten the pressure holding time, in this stage, we set the CO₂ displacement to 20 mL/min. In the middle of this stage, there were basically no AE events, and AE events did not occur until the pump pressure exceeded 7.38 MPa in 1280 s. This was mainly because CO₂ entered the supercritical state under this pressure, its diffusion capacity was significantly improved, and the primary fractures were affected by CO₂. At the same time, new micro-cracks are generated, and the pump pressure also increases rapidly as CO₂ enters the supercritical state. ③ 1550~1980 s—during the fracturing failure stage, the CO₂ injection displacement was set to 4.8 mL/min. During this stage, the pump pressure rapidly increased to the fracture pressure. At the same time, accompanied by a large number of acoustic emission events, the acoustic emission energy count rate also increased significantly. Moreover, stacking appeared, indicating that the cracks extended and expanded rapidly at this stage. In addition, due to the ultra-low viscosity and zero interfacial tension of supercritical carbon dioxide, the post-peak pump pressure curve quickly dropped to the confining pressure.

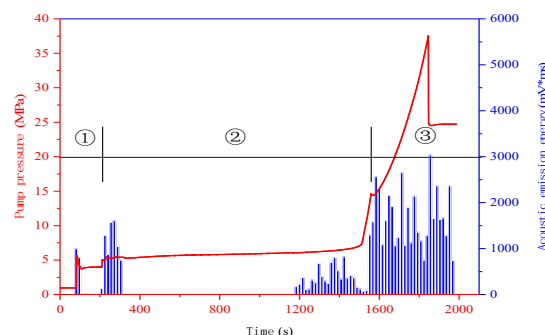


Figure 18. Pump pressure and acoustic emission characteristic curve of sample 5.

Sample 6 is No. 1956, which is taken from Well Bengyeyou 2 and is argillaceous dolomite. The photo of this sample before the experiment is shown in Figure 19. The core bedding is not developed, and the integrity of the sample is good.

The experimental confining pressure of the sample was set to 25 MPa, the axial force was 29 MPa, the displacement was 7.2 mL/min, supercritical CO₂ was used as the fracturing medium, and the sample rupture pressure was 50.77 MPa. Figure 20 shows the fracture morphology and acoustic emission location after the sample test. The acoustic emission events are mainly concentrated at the bottom of the well, indicating that the sample cracked from the bottom of the well and expanded. From the fracture morphology diagram after the sample test, it can be seen that the sample expands longitudinally after

bottom-hole fracture initiation. Because the sample bedding is not developed and the glauberite transition zone is developed in the lower part, the lithological heterogeneity causes the fracture to expand longitudinally to the lower part and bend, and finally only a curved longitudinal through-fracture is formed.



Figure 19. Core photo of sample 6 before experiment.

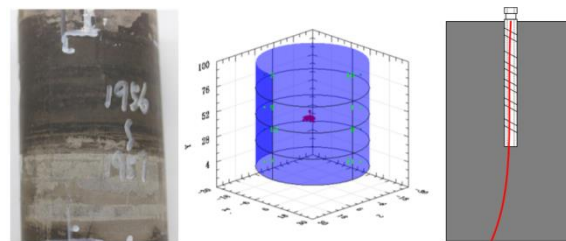


Figure 20. Core photos and acoustic emission location results of sample 6 after the experiment.

The pump pressure and acoustic emission curves are shown in Figure 21. The pump pressure curve of sample 6 can be divided into the following three stages. ① 0~120 s is the initial stage of fracturing. With the increase in the CO₂ injection rate, its inertia is significantly enhanced, and CO₂ gas rapidly fills into the non-pore space of the sample, accompanied by the generation of partial acoustic emission events. ② 120~1120 s is the wellbore pressure holding stage. At this stage, fluid pressure accumulation is still relatively gentle, but the number of AE events increases significantly with the increase in the wellbore cumulative fluid injection amount, indicating that fracture initiation and propagation of the sample's primary fractures begin under the action of CO₂, but no coherent macro-fractures are formed at this stage. ③ 1120~1420 s is the fracturing failure stage. With the continuous increase in the liquid injection volume, the pressure of supercritical CO₂ also increases rapidly. When the wellbore pressure reaches 50.77 MPa, the sample is unstable and fails. Due to the ultra-low viscosity and zero interfacial tension of supercritical CO₂, the pump pressure curve rapidly drops to the confining pressure.

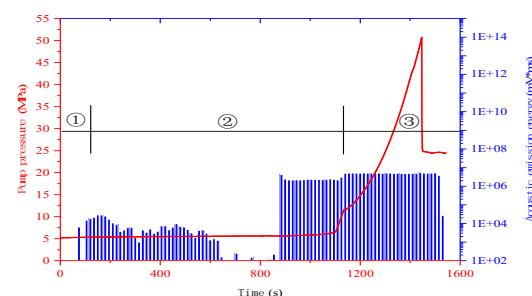


Figure 21. Pump pressure curve of sample 6.

Sample 7 is No. 25-SC; this sample is a shale outcrop, the coring direction is perpendicular to the bedding plane, the confining pressure is set to 25 MPa, the axial force is 28 MPa, the displacement is 6.0 mL/min, supercritical CO₂ is used as the fracturing medium, and the sample rupture pressure is 37.4 MPa.

The photo of the sample after the sample test is shown in Figure 22. The compression fracture is mainly composed of one longitudinal main fracture and two horizontal bedding fractures. The longitudinal main fractures are symmetrically distributed in the middle and lower parts of the sample, undergoing stratification and termination.

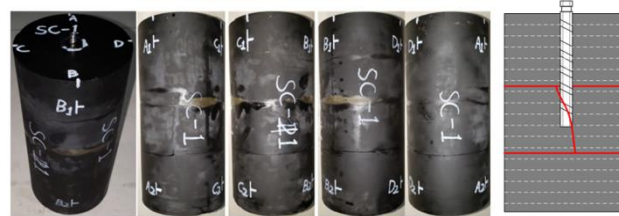


Figure 22. Core photos and acoustic emission location results of sample 7 after the experiment.

The sample pump pressure curve is shown in Figure 23. According to the pump pressure–time curve, the fracture pressure was 37.4 MPa, and after reaching the fracture pressure, it dropped rapidly to around 25 MPa, roughly equivalent to the confining pressure, indicating that the pressure crack was fully opened and penetrated the sample surface, and then dropped rapidly to approximately 20 MPa. This is due to the subsequent injection of supercritical CO₂ through the fracture to the surface of the sample along the two levels, coupled with ultra-low viscosity and zero interfacial tension of supercritical CO₂; the sand carrying capacity of supercritical CO₂ is weak and the support effect is poor, and the pressure in the fracture gradually decreases.

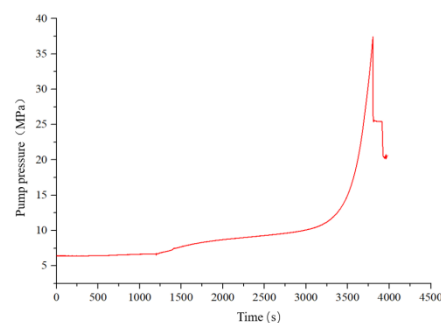


Figure 23. Pump pressure curve of sample 7.

Sample 8 is No. 26-SC; this sample is a shale outcrop, the coring direction is perpendicular to the bedding plane, the confining pressure is set to 25 MPa, the axial force is 31 MPa, the displacement is 6.0 mL/min, supercritical CO₂ is used as the fracturing medium, and the sample rupture pressure is 52.6 MPa.

The photo of the sample after the test is shown in Figure 24. One longitudinally symmetrical main crack and two bedding seams were observed on the surface of the sample. One of the bedding seams was completely opened, and the other was less than half open. The main crack has a large opening and ends at the bedding crack in the lower part of the sample during the longitudinal expansion.



Figure 24. Core photos and acoustic emission location results of sample 8 after the experiment.

The sample pump pressure curve is shown in Figure 25. From the pump pressure–time curve, it can be seen that the rupture pressure of the sample is 52.6 MPa, and after reaching the rupture pressure, it quickly drops to around 25 MPa, which is roughly equivalent to the confining pressure, indicating that the pressure cracks are fully opened and have penetrated to the surface of the sample.

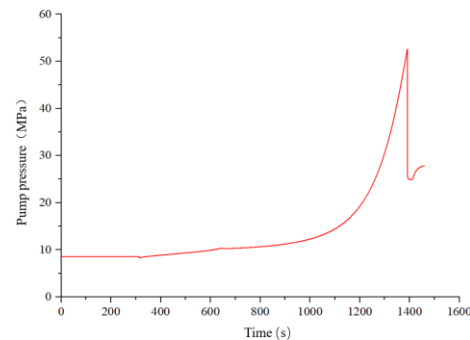


Figure 25. Pump pressure curve of sample 8.

Sample 9 is No. 27-SC; this sample is a shale outcrop, the coring direction is perpendicular to the bedding plane, the confining pressure is set to 15 MPa, the axial force is 18 MPa, the displacement is 6.0 mL/min, supercritical CO₂ is used as the fracturing medium, and the sample rupture pressure is 31.6 MPa.

The photo of the sample after the test is shown in Figure 26. A longitudinal crack is formed on the surface of the sample. The crack extends downward to the bedding plane and turns and expands along the bedding plane, and the crack opening is small.



Figure 26. Core photos and acoustic emission location results of sample 9 after the experiment.

The sample pump pressure curve is shown in Figure 27. It can be seen from the pump pressure curve that the rupture pressure of the sample is 31.6 MPa. After reaching the rupture pressure, the pump pressure curve rapidly drops to the confining pressure of approximately 15 MPa, and the sample is damaged, forming a longitudinal bedding joint and a horizontal bedding joint. All penetrated to the surface of the sample, and then dropped rapidly to around 7 MPa. This is because of the subsequent injection of supercritical CO₂ along the two through-fractures to the surface of the sample, coupled with the ultra-low-viscosity and zero interfacial tension of supercritical CO₂; the supercritical CO₂ has a weak sand-carrying ability and poor supporting effect, and the pressure in the fracture gradually decreases.

Sample 10 was designated 28-SC. The sample is a shale outcrop, the coring direction is perpendicular to the bedding plane, the confining pressure is set to 25 MPa, the axial force is 28 MPa, the displacement is 1.2 mL/min, supercritical CO₂ is used as the fracturing medium, and the sample rupture pressure is 34.5 MPa.

The photo of the sample after the test is shown in Figure 28. The pressure crack is composed of one unilateral main seam and three bedding seams. The main seam is in the form of a single wing, which only appears on one side of the sample, and no cracks are found on the symmetrical side. Among the bedding seams, only one is fully open, and the other two are open in a small area. The opening of the main crack is small, and the crack is relatively fine.

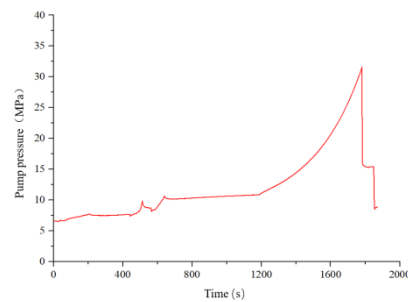


Figure 27. Pump pressure curve of sample 9.



Figure 28. Core photos and acoustic emission location results of sample 10 after the experiment.

The sample pump pressure curve is shown in Figure 29. It can be seen from the pump pressure curve that the rupture pressure of the sample is 34.5 MPa. After reaching the rupture pressure, the pump pressure curve decreases slowly, and finally drops to around 25 MPa, which is the same as the confining pressure. This is because, after the longitudinal cracks and horizontally opened bedding fractures of the sample extend to the surface of the sample, there are still other horizontal bedding fractures opened in a small range, so the pump pressure curve decreases slowly.

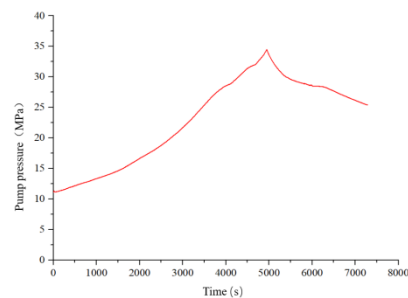


Figure 29. Pump pressure curve of sample 10.

4. Discussion

4.1. Fracturing Fluid Viscosity

Figures 4, 10 and 17 show the post-test crack propagation characterization pictures of sample 1, sample 3, and sample 5. By comparing the post-pressing photos, CT scan results, and AE acoustic emission localization results of the three samples, it can be seen that, under low-displacement conditions, the high-viscosity guar gum fracturing fluid opened many horizontal fractures with larger fracture widths, while the low-viscosity slick water fracturing fluid and the lower-viscosity supercritical carbon dioxide fracturing fluid only opened one horizontal bedding fracture and one curved longitudinal fracture, and the fracture width gradually decreased. This is due to the influence of the development degree of bedding planes in the actual core used in the experiment. Sample 1 is a bedded shale, but only contains one. The strips open the bedding plane, so only one horizontal bedding seam is opened. Sample 5 is argillaceous dolomite. The surface of the sample is filled with glauberite and other minerals, but no obvious bedding fractures are observed. In addition, the supercritical carbon dioxide has a weak sand-carrying ability, and some fractures with

small widths may be compressed. Closure occurs, so only one longitudinal expansion seam with a curved lower half is formed after pressing. However, it can be seen from the CT scan and AE acoustic emission location points that both samples contain a large number of expanding horizontal bedding fractures. Even if the geological conditions of the actual core itself are excluded, it can still be shown that the low-viscosity fracturing fluid is easier to open. There are lots of bedding cracks. The larger fracture width of the high-viscosity fracturing fluid is mainly because the sand-carrying ability and fracture-supporting ability increase with the increase in fracturing fluid viscosity, and the fracture width increases after fracturing. The supercritical carbon dioxide fracturing fluid has low viscosity and poor sand-carrying ability, and it has the weakest ability to support fractures, resulting in the smallest fracture width and even closure. The acoustic emission and pump pressure curves of the three samples are shown in Figures 5, 11 and 18. The supercritical carbon dioxide fracturing fluid, slick water fracturing fluid, and guar gum fracturing fluid reach the rupture pressure for 1780 s, 860 s, and 580 s, respectively, and the achieved burst pressures are 37.55 Mpa, 27.57 Mpa, and 27.89 Mpa, respectively. By comparison, it can be seen that under the condition of low displacement, with the increase in fracturing fluid viscosity, the time for macroscopic failure of the sample gradually decreases, and the fracture pressure during failure gradually increases. This is because, as the viscosity of the fracturing fluid increases, the permeability decreases, and the pressure rise time of the fracturing fluid in the bottom hole and fractures is shortened, so the time for reaching the bottom-hole fracture initiation pressure and promoting fracture expansion to reach the failure pressure is shortened; however, due to the viscosity, the increase leads to a faster rate of pressure rise, which is also accompanied by an increase in rupture pressure when the specimen fails. Although supercritical carbon dioxide fracturing fluid has the characteristics of low viscosity and high diffusivity, it is easy to activate the natural bedding surface, but due to its poor sand-carrying ability and strong permeability, the pressure holding time is the longest, and it also reaches the time of failure. The rupture pressure is also the highest. The failure of the sample causes the pump pressure curve to drop rapidly to the confining pressure after the fracture. Due to the ultra-low viscosity of supercritical carbon dioxide, zero interfacial tension, poor sand-carrying ability, and strong permeability, the drop is the fastest and the largest. At the same time, the acoustic emission events of the slick water and supercritical carbon dioxide fracturing fluid are mainly concentrated in the stage before and after the fracturing pressure, while the acoustic emission events of the guar fracturing fluid are relatively dense throughout the pump pressure curve, indicating that the fracturing fluid under low-viscosity conditions causes hydraulic fractures to be formed and expanded after the bottom is held back to a certain extent, while the high-viscosity fracturing fluid can communicate and generate a large number of micro-cracks at the beginning of fracturing fluid injection.

Figures 7, 14 and 20 show the post-test crack propagation characterization pictures of sample 2, sample 4, and sample 6. By comparing the post-pressing photos, CT scan results, and AE acoustic emission localization results of the three samples, it can be seen that under the condition of high displacement, the high-viscosity guar gum opened many horizontal fractures after the hydraulic fracturing, and the low-viscosity guar gum opened many horizontal fractures. After the slick water fracturing hydraulic pressure, multiple horizontal fractures were opened, while the lower-viscosity supercritical carbon dioxide fracturing fluid only had one curved vertical fracture, which is the same as the case of sample 5, both of which are due to the same geological downhole core due to constraints. Excluding actual core conditions, it can be shown that both low-viscosity fracturing fluids and high-viscosity fracturing fluids can open a large number of bedding fractures. At the same time, the acoustic emission and pump pressure curves of the three samples shown in Figures 8, 15 and 21 are compared. At 1380 s, 220 s, and 117 s, the achieved burst pressures were 50.77 Mpa, 32.35 Mpa, and 30.97 Mpa, respectively. According to the analysis, we can derive the same law as the viscosity change of the fracturing fluid under low-displacement conditions, while, under high-displacement conditions, the slick water and supercritical

carbon dioxide fracturing fluid have some intensive acoustic emission events in the initial stage of fracturing fluid injection, due to increased displacement.

4.2. Ground Stress

As the influence of ground stress on the law of hydraulic fracture propagation of conventional slick water fracturing fluid and guar gum fracturing fluid is relatively clear, supercritical carbon dioxide, with unique properties, was selected as the fracturing fluid in this experiment to study the influence of ground stress on the law of hydraulic fracture propagation. Sample 7, sample 8, and sample 9 are shale outcrops of Well Bangyeyou 2, and the three groups of in-situ stress combinations are axial pressure = 28 Mpa and confining pressure = 25 Mpa; axial pressure = 31 Mpa, confining pressure = 25 Mpa; axial pressure = 18 Mpa, confining pressure = 15 Mpa, respectively. The post-test fracture characteristics of the three groups of samples are shown in Figures 22, 24 and 26. After the compression of sample 7, the fractures extend longitudinally along the bottom of the hole to connect the upper and lower salt rock thin interlayers, and then turn along the salt rock bedding plane. They expand to form two horizontal bedding seams running through. After the fracturing of sample 8, the fractures started from the bottom of the well and extended longitudinally to connect the upper and lower salt rock thin interlayers, and then turned downward and expanded along the salt rock bedding plane, and turned upward and expanded along the salt rock bedding plane while continuing to rise through the interlayer. They expanded and finally formed a longitudinal fracture penetrating upwards, a horizontal bedding fracture penetrating and a horizontal bedding fracture in the extended part. After the fracturing of sample 9, the fractures from the bottom of the well extended longitudinally to the upper and lower salt rock thin interlayers, crossed the salt rock bedding plane upwards, turned downward and expanded along the salt rock bedding plane, and finally formed a vertical line penetrating upward, with cracks and one horizontally penetrating bedding joint. From the comparison between Figures 22 and 26, it can be seen that in the case of high in-situ stress combination, the fracture will turn longitudinally to the bedding plane, and it will expand along the bedding plane and cannot pass through the bedding plane. In the case of low in-situ stress, the fractures grow longitudinally along the direction of the bedding plane, and at the same time, they attempt to pass through the bedding plane to communicate with the surface of the sample; thus, the in-situ stress decreases, and the development of the fracture network is more complex. This is mainly because with the increase in confining pressure, the brittle ductility characteristics of rock will change, the vertical stress difference coefficient will decrease, and the fracture toughness will increase significantly, resulting in an increase in the difficulty of crack initiation and the ability to prevent crack propagation; the vertical bedding plane is more difficult to penetrate, so it still leads to a decrease in fracture complexity. From the comparison of Figures 22 and 24, it can be seen that under the same confining pressure, with the increase in axial pressure, the crack can open the horizontal bedding fracture and continue to expand upward through the bedding surface and penetrate the surface of the sample. The main reason is that the axial pressure increases, the vertical stress difference coefficient increases, the fracture's ability to penetrate the bedding plane in the longitudinal direction increases, and the fracture complexity increases. Figures 23, 25 and 27 are the pump pressure curves of sample 7, sample 8, and sample 9. The rupture pressures of the three groups of samples are 37.4 Mpa, 52.6 Mpa, and 31.6 Mpa, respectively. It can be seen from the comparison that with the increase in in-situ stress, the rupture pressure gradually increases, which is mainly due to the increase in fracture toughness, which leads to the improvement in the difficulty of crack initiation and the ability to prevent crack expansion, as well as an increase in the rupture pressure.

4.3. Pump Displacement

The comparison between Figures 4, 6, 13, 16, 17 and 20, shows that, excluding the influence of the bedding plane distribution of the sample core itself, with the increase

in pumping capacity, the more bedding planes propagate through and open fractures, the more bedding cracks are formed, and the complexity of the fracture network also increases. Figures 22 and 28 are the characterization diagrams of fracture propagation after the fracturing of sample 7 and sample 10. When the fracturing fluid is supercritical carbon dioxide, the fracture longitudinally expands to connect the upper and lower salt rock thin interlayers under the condition of high pumping displacement. The diversion occurs and expands along the salt rock bedding plane. In order to pass through the bedding plane, two horizontal bedding fractures are formed. Under the condition of low pump injection rate, the fractures extend longitudinally to connect the upper and lower bedding planes, turn to expand along the bedding planes, and, at the same time, pass upward through the bedding planes and penetrate to the surface of the sample, forming three main horizontal bedding fractures and a longitudinal crack. By comparison, it can be seen that under the condition of supercritical carbon dioxide fracturing fluid, with the increase in pumping displacement, the complexity of the fracture network decreases instead. This is due to the low viscosity and high diffusion characteristics of supercritical carbon dioxide, which can easily activate natural bedding fractures. With the increase in pumping displacement, the longitudinal fractures expand to communicate with the bedding fractures and then turn to rapidly expand to the surface of the sample. The high permeability causes most of the fracturing fluid to flow out along the through-fractures, making it difficult to continue to open new fractures and form a complex fracture network. By comparing Figure 5 with Figures 8, 13, 15, 18 and 29, it can be seen that as the displacement increases, the rupture pressure gradually increases, and at the same time, some acoustic emission events appear in the early stage of the pump pressure curve; this is due to the fact that increasing the displacement leads to a faster rate of pressure hold-up at the bottom of the well at the initial stage of fracturing fluid injection, and a large number of micro-fractures are opened.

5. Conclusions

- (1) Low-viscosity slick water fracturing fluid can more easily open bedding fractures and induce complex fracture networks in the reservoir. Guar gum fracturing has high viscosity and good sand-carrying performance, so high-viscosity guar fracturing fluid can still open bedding fractures around the wellbore. Supercritical carbon dioxide has low viscosity and high diffusion characteristics, which can easily activate natural bedding fractures and induce complex fracture networks in the formation, but the fracture width is generally small. In addition, due to the weak sand-carrying capacity of supercritical carbon dioxide, the fracture support is insufficient. At the same time, with the increase in viscosity, the occurrence time of fracturing pressure decreases gradually, and the fracturing pressure gradually increases. However, the fracturing pressure of supercritical carbon dioxide is much higher than that of other types of fracturing fluid due to its strong permeability and poor sand-carrying properties.
- (2) Under the condition of pumping supercritical carbon dioxide fracturing fluid, as the in-situ stress increases, the fracture pressure of the inter-salt shale gradually increases, the brittle–ductile characteristics of the shale will change, and the fracture toughness will be significantly enhanced. The difficulty of crack initiation and the ability to prevent crack propagation increase, and the complexity of cracks decreases.
- (3) With the increase in pumping displacement, the fracture pressure of inter-salt shale gradually increases, and a large number of micro-fractures will be opened in the early stage of fracturing fluid injection. At the same time, the greater the number of cracks passing through layers and opening bedding planes, the more bedding fractures are formed, and the complexity of the fracture network also increases. However, due to the low viscosity, high diffusion characteristics, and high permeability of supercritical carbon dioxide fracturing fluid, as the displacement increases, the fractures rapidly expand to the surface of the sample to form through-fractures, and most of the fracturing fluid flows out from the through-fractures to form pressure relief zones; it is difficult to continue to open new cracks to form a complex network of cracks.

Therefore, the complexity of the seam network decreases with the increase in the displacement of supercritical carbon dioxide.

- (4) When hydraulically fracturing the inter-salt shale reservoirs in the field, a fracturing fluid with moderate viscosity should be selected as much as possible, while the pumping displacement should be increased to open more laminar fractures and form a complex fracture network. However, an excessively high pumping displacement will lead to higher fracture pressure and affect the safety of on-site construction, so a follow-up study will be carried out to investigate the influence of pumping methods and other effects on the expansion pattern of hydraulic fractures and the degree of fracture network development in inter-salt shale.

Author Contributions: Data curation, Y.S.; formal analysis, Z.H.; methodology, Z.H. and X.C.; writing—original draft, Z.H.; writing—review and editing, Y.G. and X.C. All authors have read and agreed to the published version of the manuscript.

Funding: The State Energy Center for Shale Oil Research and Development (grant no. G5800-18-ZS-KFNY001).

Institutional Review Board Statement: Not applicable.

Informed Consent Statement: Not applicable.

Data Availability Statement: Not applicable.

Acknowledgments: The authors would like to acknowledge the funding support of the State Energy Center for Shale Oil Research and Development (grant no. G5800-18-ZS-KFNY001).

Conflicts of Interest: The authors declare no conflict of interest.

References

- Vikram, V.; Mohd, R.; Bankim, M.; Pradhan, S.P.; Singh, T.N. Temperature effect on the mechanical behavior of shale: Implication for shale gas production. *Geosyst. Geoenviron.* **2022**, *1*, 100078.
- Mohyuddin, S.G.; Radwan, A.E.; Mohamed, M. A review of Pakistani shales for shale gas exploration and comparison to North American shale plays. *Energy Rep.* **2022**, *8*, 6423–6442.
- Owusu, E.B.; Tsegab, G.H. The potential of shale gas resources in Peninsular Malaysia. *IOP Conf. Ser. Earth Environ. Sci.* **2022**, *1003*, 012024. [\[CrossRef\]](#)
- Liu, H.; Xu, S.; Zhu, B.; Zhou, L.; Huang, Y.; Li, B. Research and practice of volumetric fracturing technology for inter-salt shale oil. *Spec. Oil Gas Reserv.* **2022**, *29*, 149–156.
- Shu, H. Characteristics and Comparative Analysis of Oil Reservoirs in Jiangnan Inter-salt Shale. *J. Jiangnan Pet. Staff. Univ.* **2021**, *34*, 31–33.
- Li, Y. Characteristics of inter-salt shale oil reservoirs in the Jiangnan Basin and countermeasures for their development. *J. Jiangnan Pet. Staff. Univ.* **2019**, *32*, 24–26.
- Li, B. Analysis of key factors affecting fracturing construction and rejection characteristics of inter-salt shale reservoirs. *J. Jiangnan Pet. Staff. Univ.* **2018**, *31*, 18–21.
- Zhang, Z. Evaluation of the Effectiveness of Artificial Fractures in Inter-Salt Shale Oil Reservoirs. China University of Petroleum Beijing. 2018. Available online: <https://cdmd.cnki.com.cn/Article/CDMD-11414-1019927289.htm> (accessed on 17 April 2022).
- Liu, J. Study on the Method of Evaluating the Compressibility of Inter-Salt Shale Oil Reservoirs. Chongqing University, Chongqing, China. 2018. Available online: <http://cdmd.cnki.com.cn/Article/CDMD-10611-1018853435.htm> (accessed on 17 April 2022).
- Zhang, X.; Bi, Z.; Chang, X.; Wang, L.; Yang, H. Experimental Investigation on Hydraulic Fracture Morphology of Inter-Salt Shale Formation. *Frontiers* **2021**, *9*, 893. [\[CrossRef\]](#)
- Wang, S.; Nie, H.; Ma, S.; Ding, Y.; Li, H.; Liang, W. Evaluation of inter-salt shale oil resources and sweet spot prediction in the Paleocene Qianjiang Formation, Qianjiang Depression, Jiangnan Basin. *Pet. Exp. Geol.* **2022**, *44*, 94–101.
- Wen, H.; Lu, S.; Xue, H.; Wang, W.; Li, J.; Hu, Y.; Zhang, P.; Li, J. Main controlling factors of physical development of shale oil reservoirs in The Xingouzui Formation of Jiangnan Basin. *Oil Gas Geol.* **2016**, *37*, 56–61.
- Zheng, Y. Key Technology for Enrichment Mechanism and Dessert Prediction of Onshore Shale Oil in Salt Lake Basin. Research Institute of Exploration and Development, Jiangnan Oilfield Branch. *China Pet. Chem. Corp.* **2020**, *12*, 1.
- Zhi, X.; Shu, X.; Sang, L.; Zhang, Y. Analysis of formation patterns of inter-salt argillaline dolomite in Qianjiang Formation of Qianjiang Sag. *J. Yangtze Univ. Nat. Sci. Ed.* **2012**, *9*, 19–23+4–5.
- Shi, Z.; Jiang, J. Prediction of shallow oil and gas reservoirs in Jiangnan Basin. *Oil Gas Geol.* **1988**, 204–208.
- Shi, Z.; Pan, G. Hidden reservoirs and their exploration in Qianjiang Sag in Jiangnan Salt Lake Basin. *Daqing Pet. Geol. Dev.* **1984**, 119–129. [\[CrossRef\]](#)

17. Chen, B.; Xiao, Q.; Cao, J.; Zhao, H. Comparison of exploration potential of non-sandstone oil and gas reservoirs between Qianjiang Formation and Shashi Formation in Jiangnan Basin. *Pet. Explor. Dev.* **2017**, *190*–196.
18. Yang, Z.; Li, R.; Li, H.; Luo, Y.; Chen, T.; Gao, T.; Zhang, Y. Experimental evaluation of the salt dissolution in inter-salt shale oil reservoirs. *Pet. Explor. Dev. Online* **2020**, *47*, 803–809. [[CrossRef](#)]
19. Warpinski, N.R.; Clark, J.A.; Schmidt, R.A.; Huddle, C.W. Laboratory investigation on the-effect of in-situ stresses on hydraulic fracture containment. *Soc. Pet. Eng.* **1982**, *22*, 333–340. [[CrossRef](#)]
20. Anderson, G.D. Effects of friction on hydraulic fracture growth near unbonded interfaces in rocks. *Soc. Pet. Eng.* **1981**, *21*, 21–29. [[CrossRef](#)]
21. Blair, S.C.; Thorpe, R.K.; Heuze, F.E.; Shaffer, R.J. Laboratory observations of the effect of geological discontinuities on hydrofracture propagation. In Proceedings of the 30th US Symposium on Rock Mechanics, Morgantown, WV, USA, 19–22 June 1989; pp. 433–450.
22. Blanton, T.L. An experimental study of interaction between hydraulically induced and pre-existing fractures. In Proceedings of the SPE Unconventional Gas Recovery Symposium, Pittsburgh, PA, USA, 16–18 May 1982; pp. 1–13.
23. Blanton, T.L. Propagation of hydraulically and dynamically induced fractures in naturally fractured reservoirs. In Proceedings of the SPE Unconventional Gas Technology Symposium, Louisville, KY, USA, 18–21 May 1986; pp. 1–15.
24. Daneshy, A.A. Hydraulic fracture propagation in layered formations. *Soc. Pet. Eng. J.* **1978**, *18*, 33–41. [[CrossRef](#)]
25. Chen, Z.; Chen, M.; Huang, R.; Shen, Z. Vertical expansion of hydraulic cracks in layered media. *J. Univ. Pet. Nat. Sci. Ed.* **1997**, *25*–28+34+116.
26. Suling, W.; Yiming, Z.; Minmin, J.; Yang, L. Study on the propagation mechanism of cracks in non-uniform rock formations. *Mech. Pract.* **2012**, *34*, 38–41+45.